energy&fuels

pubs.acs.org/EF

Article

Photoinduced Oxidation and Polymerization in Oil-Soluble Products and Interfacial Material from Petroleum Weathering

Joseph W. Frye-Jones, Martha L. Chacón-Patiño, Alan G. Marshall,* and Ryan P. Rodgers*

Cite This: *Energy Fuels* 2025, 39, 1031−1041

Read Online

ACCESS | Metrics & More | Article Recommendations | Supporting Information

ABSTRACT: Photooxidation is recognized as one of the major weathering processes in petroleum upon oil spills. Previous work with solar simulator microcosms has shown that petroleum weathering can be replicated in the laboratory with a variety of sample types and weathering periods. The microcosms can be scaled up to produce large amounts of photo-oxidized materials that enable subsequent chromatographic separations, which provide more comprehensive knowledge of its complex molecular composition. The work herein focuses on the use of a solar simulator to generate photo-oxidized compounds from a heavy vacuum gas oil for subsequent separations by 2 methods: modified aminopropyl silica extraction to target acidic species and extraction of interfacially active compounds via the "wet silica" method. Molecular characterization was performed by negative-ion (−) electrospray ionization ultrahigh resolution Fourier transform ion cyclotron resonance mass spectrometry (21 T FT-ICR MS). These results uniquely demonstrate that water-soluble photo-oxidation products are not the only phase that feature the products of photoirradiation-driven polymerization reactions. Separations allowed for the expansion of the molecular coverage, which revealed previously undetected species that were masked by the lower molecular weight acidic species that were preferentially ionized in the broadband analysis of unfractionated materials. Thus, the separations facilitated the detection of abundant oil-soluble photopolymerization products in acidic fractions of high carbon number and aromaticity. Interfacially active material (IM) also reveals minor polymerization products in later-eluting acidic fractions.

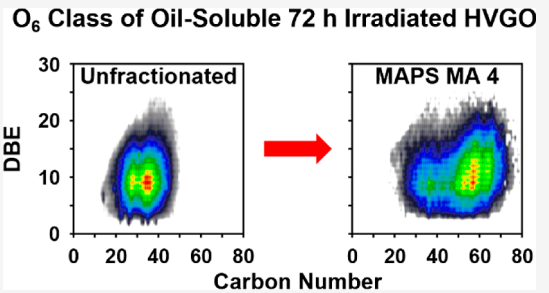

INTRODUCTION

Oil Spill Science. The 2010 Deepwater Horizon disaster sparked a decade of oil spill research focused on areas of high solar flux, such as those around the equator and the effects of environmental weathering on oil molecular composition and phase behavior in these regions. As a result, most critical weathering processes were revised to include photo-oxidation for spills that occur in these areas.[1−4] Prior to the spill in 2010, petroleum weathering was hypothesized to be dominated by evaporation immediately after the spill, followed by emulsification and biodegradation in the following hours/days. Photooxidation was not thought to begin until days/week(s) after a spill. However, several recent studies concluded that photo-oxidation is a primary weathering process along with evaporation of the lighter, more volatile compounds.[2,3,5−18] Emulsification begins hours or days after, and biodegradation does not begin until month(s) following a spill.[4,19] It should be noted that emulsification as a weathering process can result from the photochemical products generated in photo-oxidation.[20] However, it is unclear if all emulsion-stabilizing species are generated from photo-oxidation.[4] While evaporation does not create new compounds, it does lead to the increased concentration of the nonvolatile and polar species that remain.[2,4] In addition, solubilization of any water-soluble species in the native crude further increases the relative concentration of nonsoluble compounds.[2] These two processes can lead to changes in the composition for the remaining species. However, given the known compositional trends for light, medium, and heavy crude oils, such factors are unlikely in Macondo well oil (Deepwater Horizon, a light, sweet oil). While biodegradation from microbes can occur, these rarely coexist, as the processes occur stepwise.[11] Simply, photo-oxidation yields water-soluble species that have increased bioavailability. Further studies on photo-oxidation have demonstrated that it occurs more rapidly than previously thought and increases the molecular complexity (increased numbers of oxygen atoms per molecule) of petroleum only hours after solar exposure.[19] For field samples, Chen et al. investigated the molecular transformation of Macondo well oil in Louisiana saltmarsh sediments by ultrahigh resolution mass spectrometry and found that after 9 months of weathering, the recovered oil revealed ∼5.5-fold oxygen-containing (O_x) molecular formulas relative to the prespill oil.[21]

Received: June 26, 2024
Revised: November 15, 2024
Accepted: November 22, 2024
Published: January 3, 2025

Molecular-Level Analysis of Weathered Petroleum. Analysis of petroleum is routinely performed with lower resolution mass spectrometers (i.e., time-of-flight, single quadrupole, or triple quadrupole mass spectrometers) coupled to gas chromatography, which provides the identification of specific compounds within petroleum volatile and semivolatile "classes", e.g., alkanes, cycloalkanes, aromatics, sulfides, and thiophenes. However, once photo-oxidation occurs, these species are transformed into oxygen-enriched molecules with higher boiling point and decreased thermal stability, which hinders their analysis by conventional GC-based methods.[22] Thus, accurate and comprehensive molecular characterization of weathering products and nonvolatile species requires ultrahigh resolution MS, uniquely provided by high-field Fourier transform ion cyclotron resonance mass spectrometry (21 T FT-ICR MS).[23] The use of FT-ICR mass spectrometry has already demonstrated its ability to reveal the composition of ultracomplex petroleum samples (e.g., asphaltenes) and postweathering photoproducts.[8,24−30] However, there are some challenges in the routine mass spectrometry analysis of such complex mixtures. The first is that chemical functionality cannot be determined by accurate mass measurement alone, which is the key issue, since photo-oxidation generates three main oxygen-containing chemical functionalities: ketone/aldehydes, hydroxyls, and carboxylic acids.[14,31] The second is that ionization efficiency (matrix effect) will determine which species are observed by MS. Species with lower ionization efficiencies can be masked by those with higher efficiencies.[32] However, separations and chemical derivatization strategies can be used to combat both issues.[14,32]

Chemical derivatization has been used in the targeted analysis of oxygen species, more specifically ketones and aldehydes.[33] The use of Amplifex ketone derivatization agent by Niles et al. in their 2019 study highlighted ketone formation in the photoproducts by attaching a charged tag that was easily identifiable in the mass spectral data.[14] This method could be used on a whole sample but worked best in conjunction with separations to concentrate the ketones into a single fraction to reduce the potential interference with the analysis. Other methods, such as separations, can isolate the species based on oxygen functionality. A modified aminopropyl silica (MAPS) extraction demonstrated this ability to isolate acidic species based on hydrophobicity and molecular weight.[32,34,35] With this method, lower-molecular-weight acids that ionize efficiently are selectively eluted in early fractions, whereas mid-to high-molecular-weight acids are eluted in later fractions; heavier acids typically exhibit lower ionization efficiencies.[34] Thus, MAPS separation increases the molecular coverage by first isolating the easy-to-ionize compounds from those species that feature much lower ion production efficiencies. One report highlights an increase from ∼4400 assignments for an unfractionated sample to ∼13,500 unique molecular formulas assigned after fractionation.[35]

Understanding how oil-soluble petroleum molecules transition into the aqueous phase is central to oil spill science and the rational design of postspill chemical treatments and remediation strategies. The operational consequence for the transitional "phase" of emulsified crude oil is decreased effectiveness in collection and dispersion efforts in the field due to increased viscosity, water content, and molecular weight. Understanding the chemical processes that lead to this "phase" could facilitate chemical treatments to increase its dispersion and bioavailability.[4,12] However, it requires comprehensive knowledge of the molecular composition of the emulsified crude oil. Notably, photo-oxidation products can be categorized into three major solubility fractions: oil-soluble, interfacially active compounds [interfacial material, IM], and water-soluble species. Of the photoproducts, oil-solubles feature the highest carbon content and lowest abundance-weighted O/C ratios, whereas the water-solubles contain the lowest carbon number and highest O/C ratio species. Interfacially active species are a compositional intermediate in the carbon number and O/C ratios and uniquely stabilize petroleum-water emulsions.[36−38] Analysis of unweathered oil-soluble compounds is routinely performed via atmospheric pressure photoionization (APPI) FT-ICR MS, as they generally dissolve in toluene and span H, C, and heteroatom compositions with a wide range of polarizabilities, e.g., hydrocarbons and aromatics with a moderate number (0−3) of S, N, and O heteroatoms. Conversely, weathered petroleum requires additional sample preparation steps. For instance, water-soluble species can be obtained by liquid−liquid and solid-phase extraction (SPE) or by simply drying the water phase under a gentle stream of nitrogen.[29,39,40] The remnant material is then reconstituted in methanol for MS analysis via negative-ion electrospray ionization (-ESI).[29,41] Isolation of interfacially active material (IM) requires additional separation steps. The "Wet Silica" method provides a quick and easy technique for the isolation of IM from non-IM in complex matrixes such as weathered petroleum and tight water-in-oil emulsions.[42] In such a separation, water-saturated silica gel is mixed with petroleum to create a slurry that is then packed in a glass column. Compounds with no interfacial activity are eluted first with a mixture of heptane/toluene, whereas interfacially active molecules, retained in the water layers on the SiO_2 particles, are eluted with toluene/methanol. This technique can be scaled up to isolate the desired amount of IM for subsequent fractionation by other methods, such as MAPS, to address the problems associated with selective ionization (discussed earlier). A typical IM isolation requires less than 100 mg of petroleum and less than 10 g of wet silica with 1 percent of mass loading (10 mg of oil per gram of SiO_2); however, it can be scaled up to 1 g of petroleum and 100 g of wet silica.[19,42,43] With one percent mass loading of the sample, a typical IM separation can yield up to 100 mg of IM, which provides enough IM to then perform MAPS fractionation.

The work herein reveals the molecular composition and investigates the presence of potential polymerization products for oil-soluble species and IM fractions from a weathered petroleum distillation cut subjected to solar irradiation for different time periods. Specifically, an Arabian heavy vacuum gas oil (HVGO) was photo-oxidized in a solar simulator microcosm for 12, 24, and 72 h. While HVGOs may not commonly spill in the environment, their chemical characteristics make them an ideal model for studying the behavior of similar complex mixtures in a photochemical setting. The use of an HVGO allows for insights that apply to a range of similar substances that may be involved in environmental spills. The well-defined carbon number range is critical in our experimental design because it ensures that any observed change in carbon number range can be confidently attributed to the photochemical processes under investigation (photo-induced polymerization or fragmentation). A whole petroleum sample can have a wide range of carbon number species, which is undesirable due to the inability to monitor changes in carbon

https://doi.org/10.1021/acs.energyfuels.4c03107
Energy Fuels 2025, 39, 1031−1041

number, whereas HVGOs have a narrow, defined carbon number range of ~C_{20}−C_{40}. This defined range allows for the accurate assessment of the effects of solar irradiation on the HVGO, as changes in the carbon number and double bond equivalents (DBE), due to photoinduced reactions, can be easily discerned. The photoproducts were separated into water-solubles, oil-soluble compounds (noninterfacially active, non-IM), and interfacially active (IM).

Solar photo-oxidation is a critical weathering process for spilled oil, unique in its ability to rapidly produce (days) oxygen-rich products. Understanding the pathways of photo-oxidation reactions is essential for effective response strategy development and mitigation of the environmental consequences of oil spills. Recent advances in this area can be fed into and used to refine models that can better predict mass balance, response options, transport, fate, and damage assessments. Photopolymerization, an intriguing reaction pathway, transforms low-molecular-weight compounds into more complex, high-molecular-weight species, although it has been challenging to study due to issues such as aggregation and selective ionization. This work addresses these challenges by focusing on the composition of oil-soluble photoproducts and photogenerated interfacially active materials (IM), using fractionation steps to separate and identify the photopolymerized products and improve molecular-level analysis via FT-ICR MS. Additionally, MAPS separation was performed (non-IM and IM), followed by analysis using (−) ESI 21 T FT-ICR MS. The study investigates compositional changes in HVGO after photoweathering, exploring whether previously documented water-soluble photopolymerization products also occur in oil-soluble and interfacially active materials. The findings confirm significant alterations in the chemical composition of the oil due to photopolymerization, underscoring the broader implications of sunlight-driven processes in environmental chemistry and suggesting future research directions such as exploring alternative analytical techniques and examining long-term environmental effects. The exploration of the water-soluble material generated through the photo-oxidation process will be addressed in future studies.

EXPERIMENTAL METHODS

Materials. High-performance liquid chromatography (HPLC) grade dichloromethane, methanol (MeOH), toluene (Tol), and water (H_2O) were obtained from J. T. Baker (Philipsburg, NJ) and used as received. Chromatographic grade silica gel (SiO_2) was obtained from Fluka Analytical (Charlotte, NC) (80−200 mesh, pore size 60 Å) and used for Wet Silica separation. SPE cartridges of APS (Bond Elut NH_2, 2 g, 12 mL) were purchased from Agilent (Santa Clara, CA) and used for acidic compound extractions. Formic acid (LC−MS grade, Pierce from Thermo Scientific, Waltham, MA) was used for the elution of acidic fractions. Tetramethylammonium hydroxide (TMAH, 25 wt % in MeOH, Acros Organics, Waltham, MA) was used as an ionization aid during analysis.

Photooxidation of HVGO in a Solar Simulator Microcosm. Thin films were generated with 2.6 g of HVGO distillation cut from Arabian Heavy oil layered onto 400 mL of HPLC grade water in a glass dish. This cut originates from the 427−538 °C range of the distillation process and contains an approximate carbon number range from C_{20} to C_{40}. Thin films were irradiated by artificial sunlight in an ATLAS Suntest CPS solar simulator (300−800 nm, 250−765 W/m2 irradiance range, 1500 W xenon lamp)[44] for 12, 24, and 72 h. Water temperature was maintained at 26 °C during irradiation with heatsinks connected to a water chiller set at 5 °C. A dark control was covered with aluminum foil for 72 h as a comparison/control experiment and will be referred to as 0 h throughout the manuscript. It is important to note that due to the considerable sample consumption after the two separations, a single dark control aligned with the most extensive irradiation period was performed. After irradiation, the oil layer was isolated from the water and dried under a gentle stream of nitrogen gas.

Separations of Photoproducts. Two separations were used for this study as detailed in Figure 1. Photoirradiated materials from all

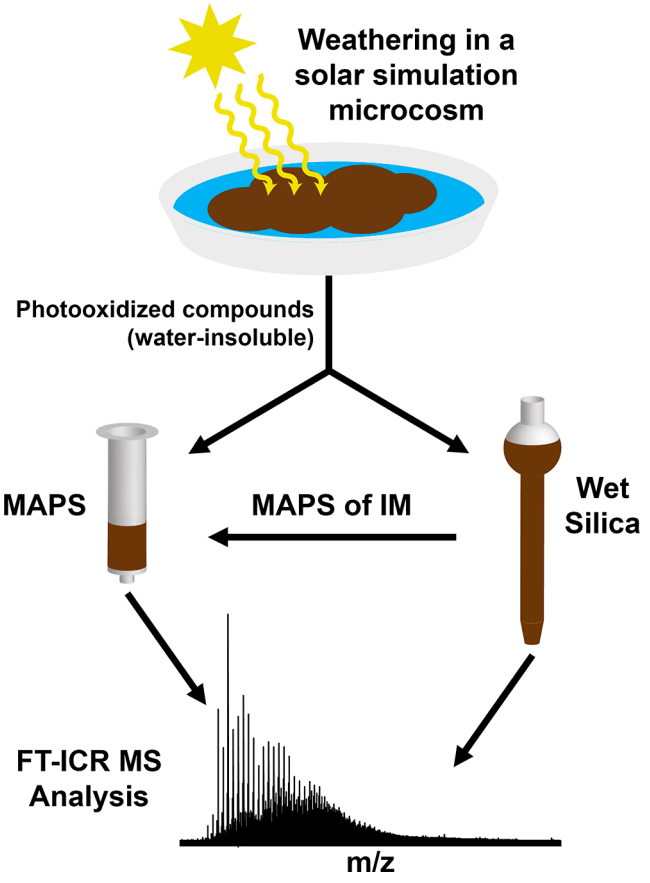

Figure 1. Experimental outline for weathering of HVGO, isolation of acidic photo-oxidized material, and IM MAPS followed by acidic species isolation before analysis by 21 T FT-ICR MS.

irradiation periods (0, 12, 24, and 72 h) were divided into two aliquots. The first aliquot was subjected to a MAPS separation for fractionation of acidic species as described previously.[34,35,45] The second aliquot was used for the isolation of the IM with the Wet Silica method. Here, dried silica gel was combined with HPLC-grade water (66% by weight) to create 100 g of water-saturated silica gel before being combined with 1 g of photo-oxidized HVGO dissolved in 50:50 heptane/toluene (v/v). Following a previously described method, the IM was isolated from the non-IM and dried under N_2.[35,42] Non-IM is eluted first with a 1:1 toluene/heptane mixture (v/v); the IM is eluted from the silica gel with toluene/MeOH 10:25 (v/v). After IM isolation, MAPS fractionation was also performed on the IM to facilitate a more complete characterization of the acidic species present. The IM is the fraction of interest from wet silica, as these species facilitate the transition from oil-soluble to water-soluble and help stabilize emulsions. Hereafter, the acronym MAPS is used for the acidic fractions derived from oil-soluble material, and IM is used for the acidic fractions from IM MAPS.

Molecular Characterization by ESI 21 T FT-ICR MS. Unfractionated photoirradiated HVGO, unfractionated IM, and the first 4 acidic fractions (MA 1−4) from both MAPS extractions were dissolved in toluene and diluted in methanol to 1 mL with a final concentration of 50−150 μg mL^{-1}, with 0.0125% TMAH spiked in to aid with deprotonation. Samples were directly infused at 0.5 μL min^{-1}

https://doi.org/10.1021/acs.energyfuels.4c03107
Energy Fuels 2025, 39, 1031−1041

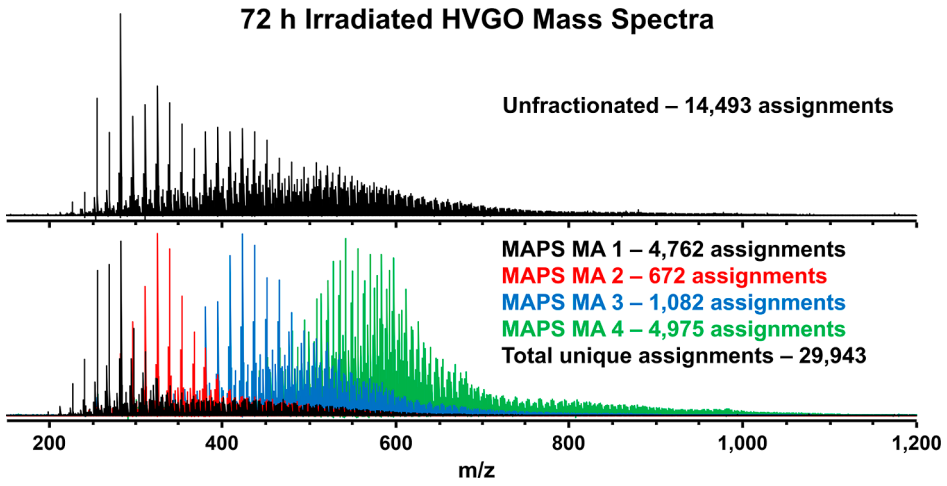

Figure 2. Mass spectra of 72 h irradiated HVGO unfractionated (top) and first 4 acidic fractions MAPS MA 1−4 (bottom) after analysis by 21 T FT-ICR MS with the number of unique molecular formula assignments found in each spectrum.

for negative-ion (−) microelectrospray ionization (ESI) coupled to a custom-built 21 T FT-ICR mass spectrometer, as previously described.[46] While other ionization modes (APPI) are preferred for petroleum analysis, (−) ESI is the optimal ionization mode for analyzing the acidic compounds, the primary target for these separations.[47] Data collection, Fourier transformation, phase correction, external calibration, peak picking, molecular formula assignment, and data visualization were performed with custom Predator and PetroOrg software.[8,48,49]

Mass spectra are externally calibrated with homologous Kendrick series of CH_2 spacings,[50] and peaks are assigned unique molecular formulas ($C_cH_hN_nO_oS_s$) based on the ultrahigh mass accuracy of FT-ICR MS. From these formulas, double bond equivalents (DBE = number of rings plus double bonds to carbon) are calculated, providing a measure of compound aromaticity.[51] Heteroatom classes are generated based on the heteroatom content for the assigned molecular formulas. For instance, all of the formulas with carbon, hydrogen, and five oxygen atoms make up the O_5 class.

RESULTS AND DISCUSSION

MAPS Extractions of Irradiated HVGO. Only the first 4 acidic fractions (MAPS MA 1−4) could be characterized by MS due to well-documented aggregation in the later fractions.[32,34,35] Previous studies have demonstrated the expansion of mass spectral coverage with the use of MAPS to target species that ionize less efficiently and have also detailed the difficulties in the MS analysis of later-eluting fractions that aggregate.[32,34,35] Figure 2 exemplifies the improved mass spectral coverage (signal/noise ratio and mass range) in the 72 h irradiated HVGO, with a comparison of the unfractionated sample mass spectrum to the first 4 acidic MAPS fractions (MA 1−4). This result is also demonstrated by the shift in the average molecular weight for each mass spectrum. The unfractionated sample reveals an average molecular weight of ∼520 Da. In comparison, MA 1 is centered around ∼400 Da, and each successive fraction shifts the average MW from ∼400 Da to a final MW ∼730 Da (MA 4). Thus, the results demonstrate that MAPS separates samples based on molecular weight/carbon content, which is related to hydrophobicity. Simply, early eluting fractions contain lower-molecular-weight acids, whereas the later-eluted fractions contain mid-to high-molecular-weight species.

Table 1 contains the monoisotopic formula assignments for the unfractionated sample and the number of unique assignments for each fraction as well as the total number of unique formulas for the acidic fractions. Here, unique assignments correspond to unique formulas found in each acidic fraction in comparison to each other. The total number corresponds to the combined unique assignments across all 4 fractions for each irradiation to demonstrate the increased compositional coverage provided by the fractionation over the unfractionated sample. Specifically, after calibration and assignments, the unfractionated sample from the 72 h irradiated HVGO revealed 14,493 monoisotopic molecular formulas, whereas combined MAPS MA 1−4 fractions featured 29,943 unique compositions. A comparison of the unique assignments shows that less than 24% are shared between MA 1 and MA 4. Thus, the results indicate that MAPS improved the compositional range accessibility relative to the unfractionated photoproducts.

Table 1. Total Assigned Monoisotopic Elemental Compositions for Unfractionated Samples from Dark Control and 12, 24, and 72 h Irradiated HVGO, as Well as the Unique Monoisotopic Elemental Compositions Assigned for the First 4 Acidic Fractions and the Total Number of Unique Compositions Assigned between all Four Fractions at Each Irradiation Period

time[a]	unfractionated[b]	MA 1[c]	MA 2[d]	MA 3[e]	MA 4[f]	total[g]
0 h	11,597	2674	666	1593	1485	19,159
12 h	17,371	3563	465	1444	4441	31,480
24 h	19,425	3861	707	1034	6662	35,395
72 h	14,493	4762	672	1082	4975	29,943

[a]Time periods of irradiation, [b]The number of monoisotopic elemental assignments from unfractionated irradiated HVGO at each time point. [c]Monoisotopic formulas unique to each acidic fraction; first acidic fraction. [d]Monoisotopic formulas unique to each acidic fraction; second acidic fraction. [e]Monoisotopic formulas unique to each acidic fraction; third acidic fraction. [f]Monoisotopic formulas unique to each acidic fraction; fourth acidic fraction. [g]Total unique monoisotopic molecular formula across all four acidic fractions.

Molecular Composition of Oil-Soluble Photoproducts. A comparison of oxygen heteroatom class distribution for the unfractionated oil-soluble HVGO photoproducts in Figure 3a, at each irradiation period, displays a shift from O_1 as the dominant oxygen heteroatom class to O_2 after just 12 h of irradiation. The O_2 class persists as the most abundant species for the remaining irradiation periods, with the 72 h time point

https://doi.org/10.1021/acs.energyfuels.4c03107
Energy Fuels 2025, 39, 1031−1041

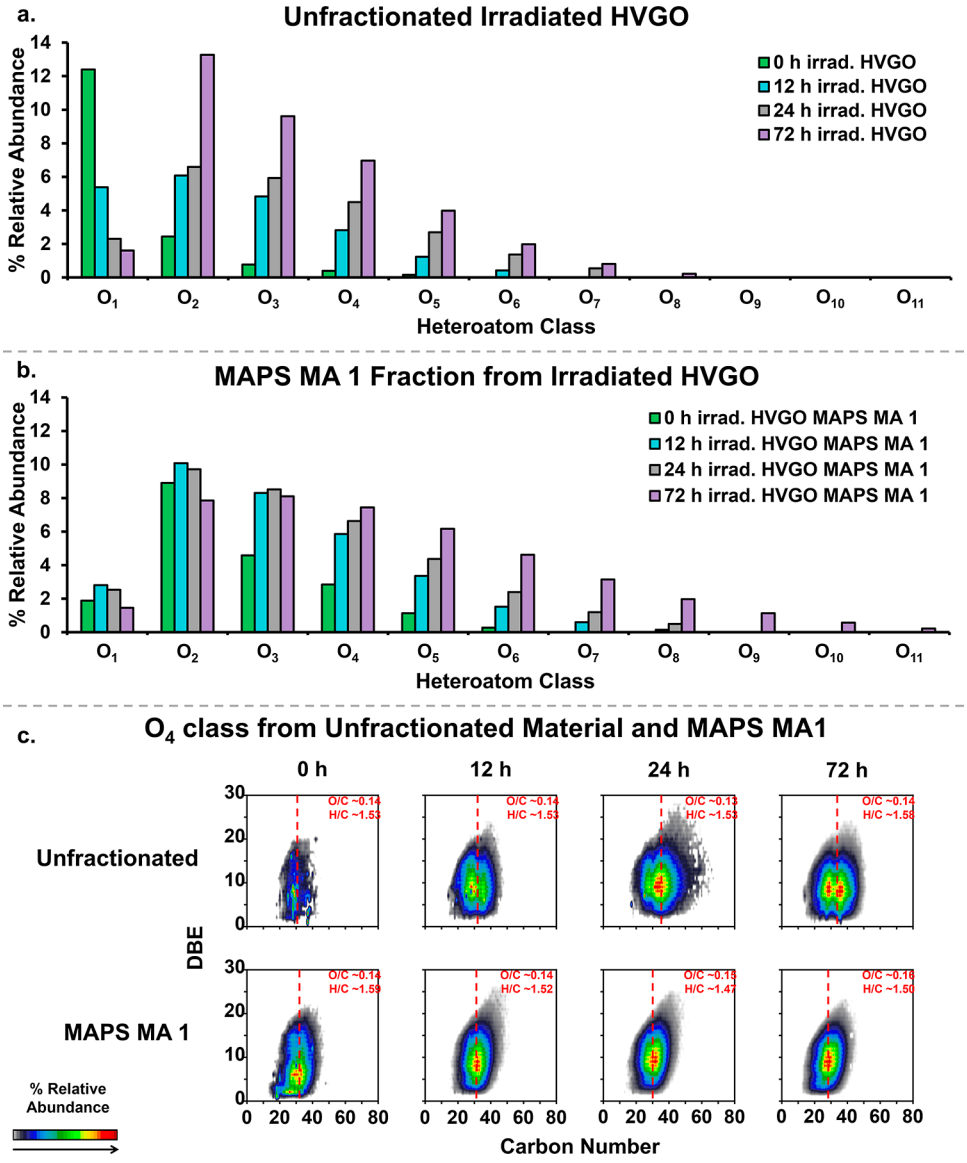

Figure 3. (a) Oxygen heteroatom class distribution for unfractionated samples at all irradiation periods, (b) oxygen heteroatom class distribution for the first acidic fraction for all irradiation periods, and (c) isoabundance color-contoured plots of DBE versus carbon number for the O_4 class of unfractionated material vs first acidic fraction derived from (−) ESI 21 T FT-ICR MS.

featuring the highest degree of photo-oxidation, up to O_8. Each additional oxygen atom increases the abundance-weighted O/C ratio of the photoproducts, whereas the abundance-weighted H/C stays relatively similar, indicating that there is very little change in the aromaticity of unfractionated species. Isolation of low-molecular-weight acidic species in the first MAPS fraction (MA 1), displayed in Figure 3b, shows that the products from 0 to 24 h irradiation periods peak in relative abundance in the O_2 class, as would be expected for acidic species. However, the 72 h irradiation exhibits abundant O_3 species, indicating that longer irradiation periods cause an increase in the oxygen content. MA 1 from the dark control (0 h) displays moderate oxygen content, starting at O_1 and extending to O_6, with a dominance of the O_2 and the O_3 species (16.2% RA), and an abundance-weighted O/C of 1.66. However, after 72 h of weathering, significant photo-oxidation occurred and molecules with up to 11 oxygen atoms were detected. Unlike the unfractionated samples, MA 1 demonstrates a peak in the abundance-weighted H/C of ∼1.71 in the O_2 class before falling to ∼1.28 in the O_{11}. The abundance-weighted O/C ratio shows an increase similar to that seen in the unfractionated sample, starting at ∼0.04 in the O_1 class to 0.31 in O_{11}. Figure 3c presents the DBE vs carbon number plots for the O_4 class for the unfractionated samples and MAPS MA 1 fractions. The unfractionated samples more closely feature the characteristic C_{20}−C_{40} carbon number range of a HVGO (427−538 °C), with limited species assigned in the dark control (no photo-oxidation, 0 h) and a bimodal distribution of molecules for all irradiation periods (most evident at 72 h). This was the lowest oxygen class that best demonstrates this bimodal distribution across the 3 irradiation time points. The first distribution is at lower C# (centered at ∼29), and the second one is centered at C# ∼36. The higher C# distribution exhibits higher relative abundance at longer irradiation periods. The abundance-weighted O/C ratios of the unfractionated sample are relatively constant across the irradiation periods at 0.13−0.14. It is interesting to note that MAPS MA 1 fractions for all irradiation periods feature only

https://doi.org/10.1021/acs.energyfuels.4c03107
Energy Fuels 2025, 39, 1031−1041

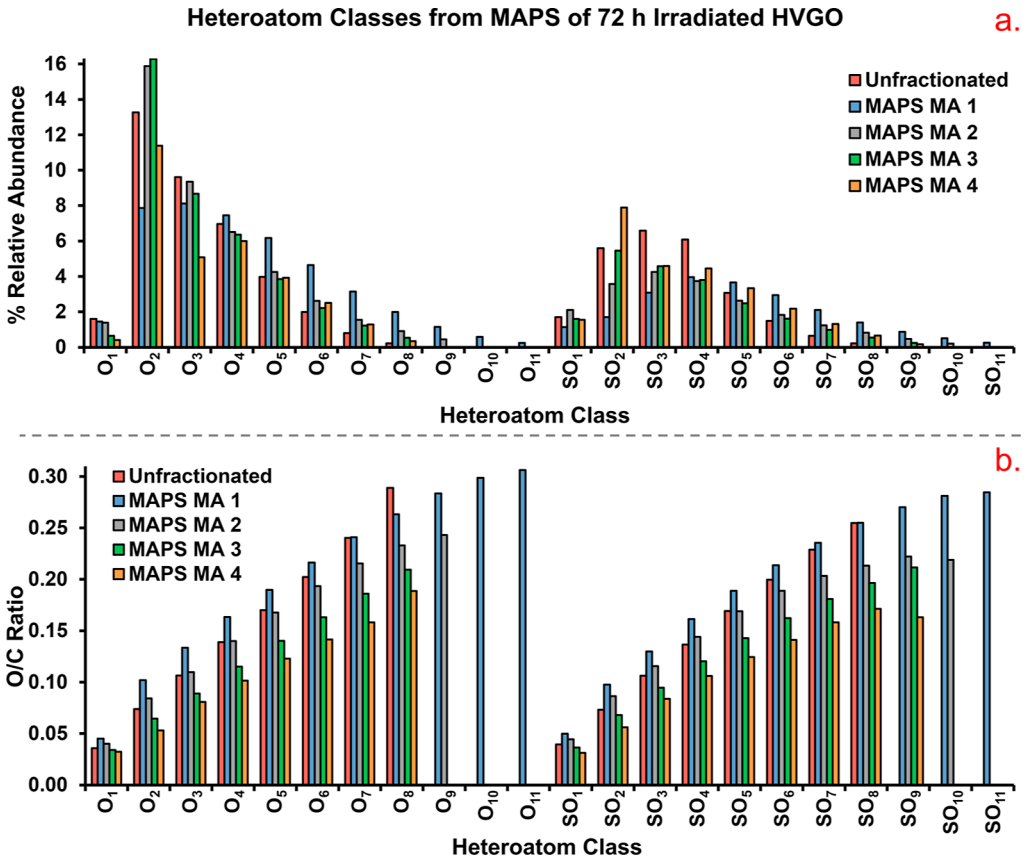

Figure 4. (a) O_x and SO_x heteroatom class distribution for 72 h irradiated HVGO unfractionated and first four acidic fractions after analysis by (−) ESI 21 T FT-ICR MS. (b) Abundance-weighted O/C ratios for O_x and SO_x heteroatom classes of 72 h irradiation HVGO unfractionated and first 4 acidic fractions.

species within C_{20}−C_{40} range, which agrees with the fact that early eluting fractions are less hydrophobic and, thus, contain fewer C atoms in alkyl chains. The increase in the irradiation period results in an increase in abundance-weighted O/C from 0.14 to 0.16 for the O_4 class. Additional values can be found in the processed data freely available through the OSF link. While there is not much statistical variation in these ratios, a general trend is highlighted which supports the increase in DBE values of the most abundant compositions. Found in Table S1 (top) are the heteroatoms assigned for the unfractionated and acidic fractions in each irradiation. Similar trends are observed in Figure S1 for the SO_x species. There is some shift in the peak oxygen class from the O_2 class for the O_x classes to S_1O_{3-4} for the SO_x compounds for the unfractionated class (Figure S1a). This trend is carried through to the first fraction with a shift to S_1O_{3-4} for all irradiation periods. In Figure S1c, the bimodal distribution is observed for the S_1O_3 class, like the O_4 class observed in Figure 3c. The abundance-weighted O/C ratios are also relatively stable for the unfractionated sample oscillating between 0.10 and 0.11 but show an increase from 0.11 to 0.13 from the dark control to the 72 h irradiation period for the first fraction.

To investigate these trends further, a comparison of all of the analyzed MAPS fractions to that of the unfractionated sample is displayed for the 72 h time point irradiation period in Figures 4, 5, 6. Figure 4a displays the heteroatom distributions within the O_x and S_1O_x classes for the unfractionated 72 h irradiated HVGO and MAPS MA 1−4. All of the samples peak in relative abundance in the O_2 class, as would be expected for the samples dominant in acidic species. The unfractionated sample has a maximum of 8 oxygen atoms per molecule (O_8 class), whereas MA 1 reaches O_{11}. Each subsequent MA fraction reduces the maximum amount of O_x present, with MA 4 extending only up to O_8. Figure 4b illustrates this point through the comparisons of the O/C ratios. Progression from MA 1 to MA 4 reveals a decrease in the abundance-weighted O/C ratio for each successive fraction. Similar trends are seen for the SO_x classes, with the unfractionated sample featuring lower O content than MA 1. Again, each subsequent fraction contains less oxygen. These results suggest that oil-soluble, heavily oxidized species are preferentially low-molecular-weight compounds that are most abundant in fraction MA 1.

The compositional range for the O_2−O_6 classes of the dark control HVGO unfractionated and MAPS MA 1−3 in Figure S2 shows that the fractions of the dark control closely resemble the carbon number range of the unfractionated sample. In fractions MA 2 and 3, there is a minor increase in the carbon number for the O_3 and the O_4 classes. For comparison, Figure 5 presents the compositional range for the O_2−O_6 classes for the 72 h irradiated HVGO unfractionated sample and its MAPS MA 1−3 fractions. The unfractionated weathered sample reveals a carbon number range close to the typical ∼C_{20}−C_{40} range for an HVGO (427−538 °C).[52,53] Bimodal distributions in both C# and DBE are observed and become more evident as a function of the increasing oxygen number. In terms of DBE, O_2 and O_3 classes in the unfractionated HVGO reveal a bimodal nature. This trend has also been observed in the work by Rojas-Ruiz et al. in the analysis of whole

https://doi.org/10.1021/acs.energyfuels.4c03107
Energy Fuels 2025, 39, 1031−1041

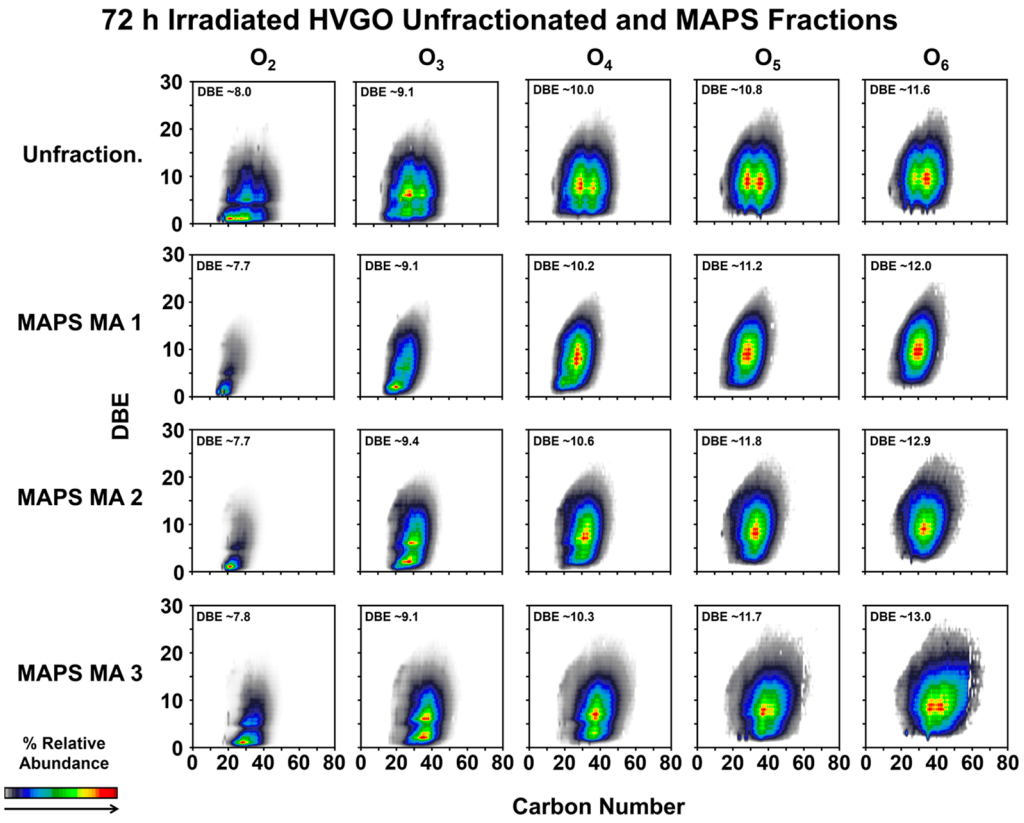

Figure 5. Isoabundance color-contoured plots of DBE versus carbon number for O_2−O_6 from 72 h irradiated HVGO unfractionated and the first 3 acidic fractions derived from (−) ESI 21 T FT-ICR MS analysis.

petroleum samples prior to the isolation of acidic species with APS.[54] The upper DBE distribution in the O_2 and O_3 classes may come from the nonacidic species in the unfractionated sample, and the lower distribution are from the lower molecular weight aliphatic type acids in early MAPS fractions. In terms of the carbon number, the most abundant compositions in the unfractionated sample shift from lower (<30, O_2/O_3 class) to higher C# (>35, O_5/O_6 class).

As previously pointed out, the bimodal distribution is not present in the acidic MAPS fractions. However, between O_2 and O_4 classes, the DBE increases indicating a shift in aromaticity from more aliphatic to more aromatic-type compounds. DBE also grows with the increase in oxygen atoms present, with the O_2 class have lower DBE than the O_6 class. This feature is present in both the acidic and unfractionated samples. Closer examination of the compositions with maximum relative abundances for MA 1−3 at higher oxygen content (O_{3-6}) shows consistency with the high-carbon-number species in the unfractionated sample, this indicating that the species isolated in MAPS MA 1−3 are represented in the unfractionated sample and ionize efficiently. Once again, similar trends are seen in the O_x for the 12 and 24 h irradiations (Figures S3−S4). The S_1O_x class demonstrates slightly different trends compared to those of the O_x. The dark control in Figure S5 exhibits a carbon number range closer to that of C_{20}−C_{40} across the unfractionated and acidic fractions. After 12 h of irradiation (Figure S6), the later acidic fractions demonstrate some extension to higher carbon number species. These trends continue into the 24 and 72 h irradiations in Figures S7−S8.

On the other hand, MAPS MA 4 displays (Figure 6, upper panel) a much more extended compositional range in the irradiated samples that are not present in the dark control (Figure S9). The class of O_1 features the C_{20}−C_{40} carbon number range, but each successive oxygen atom added shifts the compositional range to higher carbon numbers. The carbon number range for the O_6 class is C_{30}−C_{75}, nearly 2-fold higher than that of a typical 427−538 °C HVGO.[52,53] This trend is not unique to the longest irradiation period, as both 12 and 24 h time points also display this feature (Figures S10−S11). Previous MAPS studies with whole oils demonstrate a whole carbon number range shift throughout the MAPS separations, from C_{10} through C_{90}.[34,35] This highlights the necessity of a narrow distillate cut for this study, as the whole oil could mask any potential molecular changes occurring from photochemical reactions. The increase in the carbon number observed here could be attributed to polymerization (addition) reactions occurring in the oil-soluble species. The potential pathway for photo-oxidation and photopolymerization is suggested in the lower panel of Figure 6. Smaller central ring structures with alkyl side chains are photo-oxidized and polymerized to form the higher carbon number structures observed. A few studies have demonstrated the role of photochemically driven fragmentation and polymerization in the molecular composition of water-soluble species generated from weathering of petroleum products, but this data suggest that it may not be limited to water-soluble compounds, as it is readily observed in the oil-soluble fractions after MAPS fractionation.[29,55,56] The photo-oxidation process may suggest potential pathways for this formation through direct and indirect photolysis. Larger aromatic cores may undergo direct photolysis by the absorption of energy from light to cleave bonds or initiate the polymerization process like the radical oxygen photo-oxidation process. Photolysis may be induced

https://doi.org/10.1021/acs.energyfuels.4c03107
Energy Fuels 2025, 39, 1031−1041

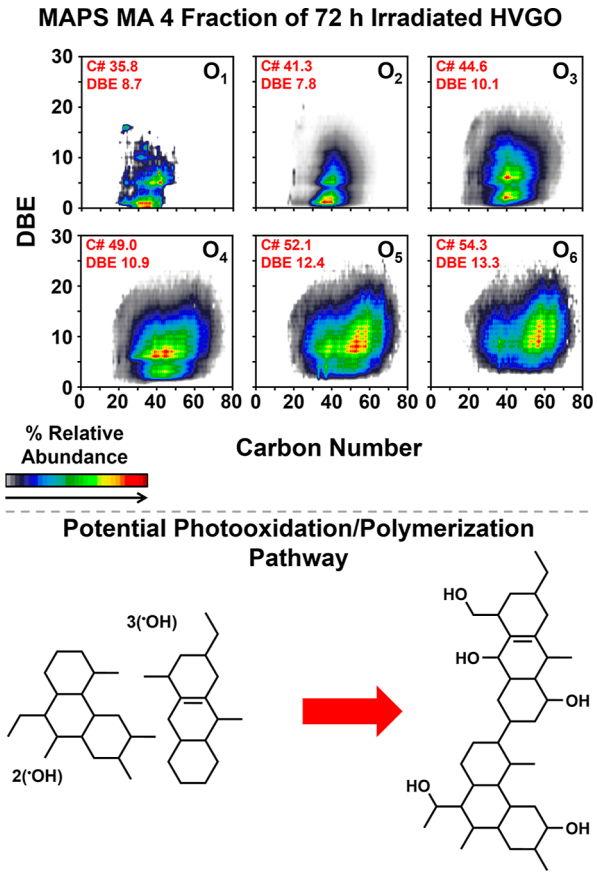

Figure 6. Isoabundance color-contoured plots of DBE versus carbon number from O_1 to O_6 from the fourth acidic fraction of 72 h irradiated HVGO after (−) ESI 21 T FT-ICR MS (upper). Potential photo-oxidation/polymerization pathway based off a possible structure for $C_{37}H_{62}O_5$ with a DBE of 7 (lower).

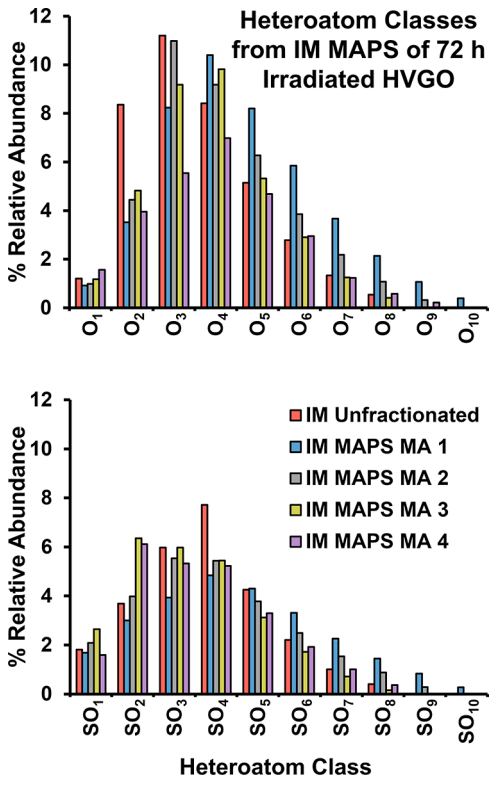

Figure 7. Heteroatom class distribution of O_x (top) and SO_x (bottom) for 72 h irradiated HVGO unfractionated IM and the first 4 acidic IM fractions after analysis by (−) ESI 21 T FT-ICR MS.

through indirect methods with smaller aromatic cores similar to singlet oxygen photo-oxidation pathways.[4] The unfractionated dark control in Figure S2 demonstrates a wide range of aromaticity from small aromatic (low DBE) to large aromatic (high DBE) cores across the oxygen species observed. This provides the starting point for these photopolymerization products to form, in addition to the photo-oxidation processes.

Isolation of Interfacial Material and Fractionation by MAPS. To investigate further if polymerization reactions are a "continuum" feature in all solubility fractions from weathered petroleum, IM was isolated from photo-oxidized HVGO, and MAPS fractionation was performed to extend its characterization. Table S1 (lower) demonstrates all of the heteroatom assignments across the unfractionated and acidic fractions for each irradiation time period. The O_x and S_1O_x heteroatom class distribution in Figure 7 shows that all fractions for the 72 h irradiated HVGO IM MAPS reveal trends in oxygen content similar to their oil-soluble counterparts (shown in Figure 4). However, the classes with the highest relative abundances have shifted from O_2 for MAPS (oil-soluble) to O_3−O_4 for IM MAPS, indicating that IM is slightly enriched in species with a higher oxygen content. The SO_x compounds exhibit a similar increase in the oxygen content with a shift from SO_2−SO_3 in MAPS to SO_3−SO_4 in IM MAPS.

Regarding the compositional range, the unfractionated IM and IM MAPS MA 1−3 feature DBE versus carbon number plots with trends similar to those presented in Figure 5. The data are included in Supporting Information, Figures S12−S15. Specifically, the fractions reveal a bimodal distribution, evident for the higher oxygen-containing species for the unfractionated IM. Such bimodal composition in carbon number is not observed in IM MA 1−3 fractions. Again, the hotspots (compositions with the highest relative abundance) for IM MA 1−3 line up with the hotspots in the bimodal distribution of the unfractionated sample. An important feature is that the O_6 class for IM MA 3 extends beyond carbon numbers typical of an HVGO C_{20}−$_{40}$ (up to C# 60). Examination of the IM MAPS MA 4 fraction from the 72 h irradiated HVGO (Figure 8) shows that the dramatic shift in the carbon number is not present in IM MA 4. The detected species mostly remain within the carbon number range typical for the unweathered HVGO. Comparison between MAPS MA 4 and IM MAPS MA 4 clearly shows that the IM MAPS does not contain the species with high carbon numbers and reveals a decrease in the abundance-weighted carbon number, whereas the MAPS demonstrates a steady increase with additional oxidation. However, earlier IM MAPS fractions have demonstrated a slight increase in carbon number/DBE, indicating the presence of polymerization products in these earlier fractions. The abundance-weighted DBE values for both MAPS and IM MAPS show an increase with the shift from O_2 to O_6. It should be noted that MAPS begins at ∼7.8 in O_2 and grows to ∼13.3 by O_6, while IM MAPS starts higher at ∼9.9 in O_2 and only slightly climbs to ∼12.7 by O_6. The IM also reveals abundant compositions close to the PAH line, which is the diagonal red dotted line in the DBE vs C# plots of Figure 8. The PAH line[22] is a compositional boundary and indicates a high abundance of highly aromatic molecules with limited alkyl-chain content. C_7 asphaltenes (heptane-insoluble petroleum species with high

https://doi.org/10.1021/acs.energyfuels.4c03107
Energy Fuels 2025, 39, 1031−1041

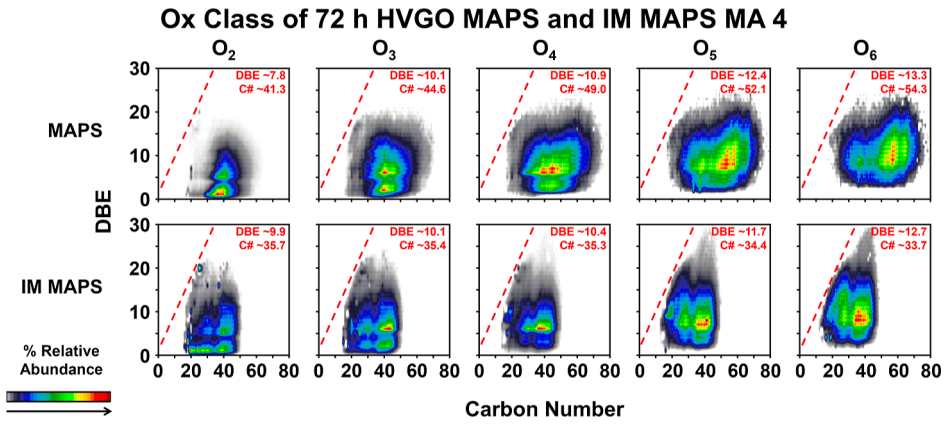

Figure 8. Isoabundance color-contoured plots of DBE versus carbon number comparing O_2 to O_6 of the fourth acidic fraction from 72 h irradiated HVGO and 72 h irradiated HVGO IM after (−) ESI 21 T FT-ICR MS analysis.

complexity) typically reveal large numbers of species near the PAH line. Thus, the data suggest that the most hydrophobic fractions from IM likely contain species with a composition consistent with that of C_7 asphaltenes. Works by Chacon-Patiño et al. and Ballard et al. have demonstrated that asphaltene fractions can also contain interfacially active material.[27,57] Those studies subjected heavy oils to asphaltene separations, followed by IM separation with the Wet Silica Method and analysis by positive APPI coupled to FT-ICR MS. The results of the analysis showed distributions in lower oxygen containing classes with PAH-like species, acylated aromatics, and aliphatic-type compounds. The IM MA 4 fraction shown in Figure 8 shows similar behavior in higher oxygen containing classes. A shift to a lower carbon number but higher DBE is present from O_4 to O_6, indicating the presence of these asphaltenic compounds in the IM. Figures S16–S17 highlight the differences between MAPS MA 4 and IM MA 4 for the dark control and 24 h of irradiation. The dark control shows similar trends as seen previously, more closely resembling a neat HVGO compositional range, while the 24 h irradiation demonstrates similar trends to the 72 h irradiation.

CONCLUSIONS

Results herein are in line with work pioneered by Chacon-Patio et al., where the first reported polymerization reactions for an Arabian heavy low boiling cut (178–283 °C) were presented. The authors focused on the water-soluble species and observed polymerization products with more than 2-fold increase in DBE and C# values. Collectively, the results presented indicate the formation of photopolymerized species in the oil-soluble phase and minor extent in the IM. The IM MAPS, with higher carbon numbers, likely transitions back to the oil phase due to their increased hydrophobicity, as was observed in IM MA 4. Moreover, the asphaltene-like species observed in the fourth acidic fraction of IM were not present in the oil-solubles or the unfractionated IM samples. This result may indicate the formation of asphaltenic species through photo-oxidation processes. However, the only the first 4 acidic fractions were analyzed due to aggregation issues that arose during analysis. Attempted analysis of acidic fractions after the fourth, resulted in continuously clogging of the ionization needle as aggregates crashed out of solution. Another limitation identified was the material required for analysis. To perform a MAPS extraction on the IM, at least 100 mg of material is required to be isolated. The yield from Wet Silica is approximately 10%, therefore at least 1 g of material had to be irradiated just for the IM isolation. Such a size of irradiation required a redesign of the microcosm experiment as a typical irradiation uses 300 mg. Despite these limitations, the experiments succeed in demonstrating the shifts in the carbon number in both the oil-soluble and interfacially active material of the HVGO analyzed.

ASSOCIATED CONTENT

Data Availability Statement

Raw FT-ICR MS data files are available at Open Science Framework (10.17605/OSF.IO/VP3U8).

Supporting Information

The Supporting Information is available free of charge at https://pubs.acs.org/doi/10.1021/acs.energyfuels.4c03107.

Heteroatom class distribution for unfractionated samples, isoabundance color-contoured plots of DBE versus carbon number, and heteroatom assignments for unfractionated and acidic fractions (PDF)

AUTHOR INFORMATION

Corresponding Authors

Alan G. Marshall − *Ion Cyclotron Resonance Program, National High Magnetic Field Laboratory, Florida State University, Tallahassee, Florida 32310, United States; Department of Chemistry and Biochemistry, Florida State University, Tallahassee, Florida 32308, United States;* orcid.org/0000-0001-9375-2532; Phone: +1 850-591-9865; Email: marshall@magnet.fsu.edu; Fax: +1 850-644-1366

Ryan P. Rodgers − *Ion Cyclotron Resonance Program, National High Magnetic Field Laboratory, Florida State University, Tallahassee, Florida 32310, United States; Department of Chemistry and Biochemistry, Florida State University, Tallahassee, Florida 32308, United States;* orcid.org/0000-0003-1302-2850; Phone: +1 850-644-2398; Email: rodgers@magnet.fsu.edu; Fax: +1 850-644-1366

Authors

Joseph W. Frye-Jones − *Ion Cyclotron Resonance Program, National High Magnetic Field Laboratory, Florida State University, Tallahassee, Florida 32310, United States; Department of Chemistry and Biochemistry, Florida State*

https://doi.org/10.1021/acs.energyfuels.4c03107
Energy Fuels 2025, 39, 1031−1041

University, Tallahassee, Florida 32308, United States; orcid.org/0000-0003-3618-8052

Martha L. Chacón-Patiño − *Ion Cyclotron Resonance Program, National High Magnetic Field Laboratory, Florida State University, Tallahassee, Florida 32310, United States;* orcid.org/0000-0002-7273-5343

Complete contact information is available at: https://pubs.acs.org/10.1021/acs.energyfuels.4c03107

Notes

The authors declare no competing financial interest.

■ ACKNOWLEDGMENTS

This work was performed at the National High Magnetic Field Laboratory Ion Cyclotron Resonance User Facility, which is supported by the National Science Foundation Division of Chemistry through Cooperative Agreement no. DMR-1644779 and the State of Florida.

■ REFERENCES

(1) Ward, C. P.; Sharpless, C. M.; Valentine, D. L.; French-McCay, D. P.; Aeppli, C.; White, H. K.; Rodgers, R. P.; Gosselin, K. M.; Nelson, R. K.; Reddy, C. M. Partial Photochemical Oxidation Was a Dominant Fate of Deepwater Horizon Surface Oil. *Environ. Sci. Technol.* **2018**, *52* (4), 1797−1805.

(2) Tarr, M. A.; Zito, P.; Overton, E. B.; Olson, G. M.; Adhikari, P. L.; Reddy, C. M. Weathering of Oil Spilled in the Marine Environment. *Oceanography* **2016**, *29* (3), 126−135.

(3) Zito, P.; Podgorski, D. C.; Bartges, T.; Guillemette, F.; Roebuck, J. A.; Spencer, R. G. M.; Rodgers, R. P.; Tarr, M. A. Sunlight-Induced Molecular Progression of Oil into Oxidized Oil Soluble Species, Interfacial Material, and Dissolved Organic Matter. *Energy Fuels* **2020**, *34* (4), 4721−4726.

(4) Ward, C. P.; Overton, E. B. How the 2010 Deepwater Horizon Spill Reshaped Our Understanding of Crude Oil Photochemcial Weathering at Sea: A Past, Present, and Future Perspective. *Environ. Sci.:Processes Impacts* **2020**, *22* (5), 1125.

(5) Aeppli, C.; Carmichael, C. A.; Nelson, R. K.; Lemkau, K. L.; Graham, W. M.; Redmond, M. C.; Valentine, D. L.; Reddy, C. M. Oil Weathering after the Deepwater Horizon Disaster Led to the Formation of Oxygenated Residues. *Environ. Sci. Technol.* **2012**, *46* (16), 8799−8807.

(6) Liu, Z.; Liu, J.; Zhu, Q.; Wu, W. The Weathering of Oil after the DeepwaterHorizon Oil Spill: Insights from the Chemical Composition of the Oil from the Sea Surface, Salt Marshes and Sediments. *Environ. Res. Lett.* **2012**, *7* (3), 035302.

(7) Hall, G. J.; Frysinger, G. S.; Aeppli, C.; Carmichael, C. A.; Gros, J.; Lemkau, K. L.; Nelson, R. K.; Reddy, C. M. Oxygenated Weathering Products of Deepwater Horizon Oil Come from Surprising Precursors. *Mar. Pollut. Bull.* **2013**, *75* (1−2), 140−149.

(8) Ruddy, B. M.; Huettel, M.; Kostka, J. E.; Lobodin, V. V.; Bythell, B. J.; McKenna, A. M.; Aeppli, C.; Reddy, C. M.; Nelson, R. K.; Marshall, A. G.; Rodgers, R. P. Targeted Petroleomics: Analytical Investigation of Macondo Well Oil Oxidation Products from Pensacola Beach. *Energy Fuels* **2014**, *28* (6), 4043−4050.

(9) Bacosa, H. P.; Erdner, D. L.; Liu, Z. Differentiating the Roles of Photooxidation and Biodegradation in the Weathering of Light Louisiana Sweet Crude Oil in Surface Water from the Deepwater Horizon Site. *Mar. Pollut. Bull.* **2015**, *95* (1), 265−272.

(10) White, H. K.; Wang, C. H.; Williams, P. L.; Findley, D. M.; Thurston, A. M.; Simister, R. L.; Aeppli, C.; Nelson, R. K.; Reddy, C. M. Long-Term Weathering and Continued Oxidation of Oil Residues from the Deepwater Horizon Spill. *Mar. Pollut. Bull.* **2016**, *113* (1−2), 380−386.

(11) Harriman, B. H.; Zito, P.; Podgorski, D. C.; Tarr, M. A.; Suflita, J. M. Impact of Photooxidation and Biodegradation on the Fate of Oil Spilled during the Deepwater Horizon Incident: Advanced Stages of Weathering. *Environ. Sci. Technol.* **2017**, *51* (13), 7412−7421.

(12) Ward, C. P.; Armstrong, C. J.; Conmy, R. N.; French-McCay, D. P.; Reddy, C. M. Photochemical Oxidation of Oil Reduced the Effectiveness of Aerial Dispersants Applied in Response to the Deepwater Horizon Spill. *Environ. Sci. Technol. Lett.* **2018**, *5*, 226−231.

(13) Zito, P.; Podgorski, D. C.; Johnson, J.; Chen, H.; Rodgers, R. P.; Guillemette, F.; Kellerman, A. M.; Spencer, R. G. M.; Tarr, M. A. Molecular-Level Composition and Acute Toxicity of Photosolubilized Petrogenic Carbon. *Environ. Sci. Technol.* **2019**, *53* (14), 8235−8243.

(14) Niles, S. F.; Chacón-Patiño, M. L.; Chen, H.; McKenna, A. M.; Blakney, G. T.; Rodgers, R. P.; Marshall, A. G. Molecular-Level Characterization of Oil-Soluble Ketone/Aldehyde Photo-Oxidation Products by Fourier Transform Ion Cyclotron Resonance Mass Spectrometry Reveals Similarity between Microcosm and Field Samples. *Environ. Sci. Technol.* **2019**, *53* (12), 6887−6894.

(15) Passow, U.; Overton, E. B. The Complexity of Spills: The Fate of the Deepwater Horizon Oil. *Annu. Rev. Mar. Sci.* **2021**, *13*, 109−136.

(16) Elsheref, M.; Messina, L.; Tarr, M. A. Photochemistry of Oil in Marine Systems: Developments since the Deepwater Horizon Spill. *Environ. Sci.:Processes Impacts* **2023**, *25*, 1878.

(17) Acter, T.; Son, S.; Kim, D.; Yim, U. H.; Barrow, M. P.; Shi, Q.; Uddin, N.; Kim, S. Environmental Petroleomics − Application of Ultrahigh-Resolution Mass Spectrometry for Molecular-Level Understanding of the Fate of Spilled Oils. *Trends Environ. Anal. Chem.* **2023**, *40*, No. e00212.

(18) Kujawinski, E. B.; Reddy, C. M.; Rodgers, R. P.; Thrash, J. C.; Valentine, D. L.; White, H. K. The First Decade of Scientific Insights from the Deepwater Horizon Oil Release. *Nat. Rev. Earth Environ.* **2020**, *1*, 237−250.

(19) Chen, H.; McKenna, A. M.; Niles, S. F.; Frye, J. W.; Glattke, T. J.; Rodgers, R. P. Time-Dependent Molecular Progression and Acute Toxicity of Oil-Soluble, Interfacially-Active, and Water-Soluble Species Reveals Their Rapid Formation in the Photodegradation of Macondo Well Oil. *Sci. Total Environ.* **2022**, *813*, 151884.

(20) Thingstad, T.; Pengerud, B. The Formation of "Chocolate Mousse" from Staffjord Crude Off and Seawater. *Mar. Pollut. Bull.* **1983**, *14*, 214−216.

(21) Chen, H.; Hou, A.; Corilo, Y. E.; Lin, Q.; Lu, J.; Mendelssohn, I. A.; Zhang, R.; Rodgers, R. P.; McKenna, A. M. 4 Years after the Deepwater Horizon Spill: Molecular Transformation of Macondo Well Oil in Louisiana Salt Marsh Sediments Revealed by FT-ICR Mass Spectrometry. *Environ. Sci. Technol.* **2016**, *50* (17), 9061−9069.

(22) McKenna, A. M.; Nelson, R. K.; Reddy, C. M.; Savory, J. J.; Kaiser, N. K.; Fitzsimmons, J. E.; Marshall, A. G.; Rodgers, R. P. Expansion of the Analytical Window for Oil Spill Characterization by Ultrahigh Resolution Mass Spectrometry: Beyond Gas Chromatography. *Environ. Sci. Technol.* **2013**, *47* (13), 7530−7539.

(23) Marshall, A. G.; Rodgers, R. P. Petroleomics: Chemistry of the Underworld. *Proc. Natl. Acad. Sci. U.S.A.* **2008**, *105*, 18090−18095.

(24) Chacón-Patiño, M. L.; Rowland, S. M.; Rodgers, R. P. Advances in Asphaltene Petroleomics. Part 1: Asphaltenes Are Composed of Abundant Island and Archipelago Structural Motifs. *Energy Fuels* **2017**, *31* (12), 13509−13518.

(25) Chacón-Patiño, M. L.; Rowland, S. M.; Rodgers, R. P. Advances in Asphaltene Petroleomics. Part 2: Selective Separation Method That Reveals Fractions Enriched in Island and Archipelago Structural Motifs by Mass Spectrometry. *Energy Fuels* **2018**, *32* (1), 314−328.

(26) Chacón-Patiño, M. L.; Rowland, S. M.; Rodgers, R. P. Advances in Asphaltene Petroleomics. Part 3. Dominance of Island or Archipelago Structural Motif Is Sample Dependent. *Energy Fuels* **2018**, *32* (9), 9106−9120.

(27) Chacón-Patiño, M. L.; Smith, D. F.; Hendrickson, C. L.; Marshall, A. G.; Rodgers, R. P. Advances in Asphaltene Petroleomics. Part 4. Compositional Trends of Solubility Subfractions Reveal That Polyfunctional Oxygen-Containing Compounds Drive Asphaltene Chemistry. *Energy Fuels* **2020**, *34* (3), 3013−3030.

(28) Chacón-Patiño, M. L.; Gray, M. R.; Rüger, C.; Smith, D. F.; Glattke, T. J.; Niles, S. F.; Neumann, A.; Weisbrod, C. R.; Yen, A.; McKenna, A. M.; Giusti, P.; Bouyssiere, B.; Barrère-Mangote, C.; Yarranton, H.; Hendrickson, C. L.; Marshall, A. G.; Rodgers, R. P. Lessons Learned from a Decade-Long Assessment of Asphaltenes by Ultrahigh-Resolution Mass Spectrometry and Implications for Complex Mixture Analysis. *Energy Fuels* **2021**, *35* (20), 16335−16376.
(29) Glattke, T. J.; Chacón-Patiño, M. L.; Marshall, A. G.; Rodgers, R. P. Molecular Characterization of Photochemically Produced Asphaltenes via Photooxidation of Deasphalted Crude Oils. *Energy Fuels* **2020**, *34* (11), 14419−14428.
(30) Lewan, M. D.; Warden, A.; Dias, R. F.; Lowry, Z. K.; Hannah, T. L.; Lillis, P. G.; Kokaly, R. F.; Hoefen, T. M.; Swayze, G. A.; Mills, C. T.; Harris, S. H.; Plumlee, G. S. Asphaltene Content and Composition as a Measure of Deepwater Horizon Oil Spill Losses within the First 80days. *Org. Geochem.* **2014**, *75*, 54−60.
(31) Takekawa, H.; Minoura, H.; Yamazaki, S. Temperature Dependence of Secondary Organic Aerosol Formation by Photo-Oxidation of Hydrocarbons. *Atmos. Environ.* **2003**, *37* (24), 3413−3424.
(32) Rodgers, R. P.; Mapolelo, M. M.; Robbins, W. K.; Chacón-Patiño, M. L.; Putman, J. C.; Niles, S. F.; Rowland, S. M.; Marshall, A. G. Combating Selective Ionization in the High Resolution Mass Spectral Characterization of Complex Mixtures. *Faraday Discuss.* **2019**, *218*, 29−51.
(33) Alhassan, A.; Andersson, J. T. Ketones in Fossil Materials - A Mass Spectrometric Analysis of a Crude Oil and a Coal Tar. *Energy Fuels* **2013**, *27* (10), 5770−5778.
(34) Rowland, S. M.; Robbins, W. K.; Corilo, Y. E.; Marshall, A. G.; Rodgers, R. P. Solid-Phase Extraction Fractionation to Extend the Characterization of Naphthenic Acids in Crude Oil by Electrospray Ionization Fourier Transform Ion Cyclotron Resonance Mass Spectrometry. *Energy Fuels* **2014**, *28* (8), 5043−5048.
(35) Clingenpeel, A. C.; Rowland, S. M.; Corilo, Y. E.; Zito, P.; Rodgers, R. P. Fractionation of Interfacial Material Reveals a Continuum of Acidic Species That Contribute to Stable Emulsion Formation. *Energy Fuels* **2017**, *31* (6), 5933−5939.
(36) Glattke, T. J.; Chacón-Patiño, M. L.; Hoque, S. S.; Ennis, T. E.; Greason, S.; Marshall, A. G.; Rodgers, R. P. Complex Mixture Analysis of Emerging Contaminants Generated from Coal Tar- and Petroleum-Derived Pavement Sealants: Molecular Compositions and Correlations with Toxicity Revealed by Fourier Transform Ion Cyclotron Resonance Mass Spectrometry. *Environ. Sci. Technol.* **2022**, *56* (18), 12988−12998.
(37) Cherney, D. P.; Wu, C.; Thorman, R. M.; Hegner, J. L.; Yeganeh, M. S.; Ferrughelli, D.; Ulysse, E. Investigating the Impact of Crude Oil Solubility on Water-in-Oil Emulsion Stability and Its Relation to Molecular Composition of Crude Oil at the Oil-Water Interface. *Energy Fuels* **2015**, *29* (6), 3616−3625.
(38) Carneiro, G. F.; Silva, R. C.; Barbosa, L. L.; Freitas, J. C. C.; Sad, C. M. S.; Tose, L. V.; Vaz, B. G.; Romão, W.; De Castro, E. V. R.; Neto, A. C.; Lacerda, V. Characterisation and Selection of Demulsifiers for Water-in-Crude Oil Emulsions Using Low-Field 1H NMR and ESI-FT-ICR MS. *Fuel* **2015**, *140*, 762−769.
(39) Subramanian, D.; May, N.; Firoozabadi, A. Functional Molecules and the Stability of Water-in-Crude Oil Emulsions. *Energy Fuels* **2017**, *31* (9), 8967−8977.
(40) McKenna, A. M.; Chen, H.; Weisbrod, C. R.; Blakney, G. T. Molecular Comparison of Solid-Phase Extraction and Liquid/Liquid Extraction of Water-Soluble Petroleum Compounds Produced through Photodegradation and Biodegradation by Ft-Icr Mass Spectrometry. *Anal. Chem.* **2021**, *93* (10), 4611−4618.
(41) Dittmar, T.; Koch, B. P.; Hertkorn, N.; Kattner, G. A Simple and Efficient Method for the Solid-Phase Extraction of Dissolved Organic Matter (SPE-DOM) from Seawater. *Limnol. Oceanogr.:Methods* **2008**, *6* (6), 230−235.
(42) Chacón-Patiño, M. L.; Niles, S. F.; Marshall, A. G.; Hendrickson, C. L.; Rodgers, R. P. Role of Molecular Structure in the Production of Water-Soluble Species by Photo-Oxidation of Petroleum. *Environ. Sci. Technol.* **2020**, *54*, 9968−9979.
(43) Jarvis, J. M.; Robbins, W. K.; Corilo, Y. E.; Rodgers, R. P. Novel Method to Isolate Interfacial Material. *Energy Fuels* **2015**, *29* (11), 7058−7064.
(44) Clingenpeel, A. C.; Robbins, W. K.; Corilo, Y. E.; Rodgers, R. P. Effect of the Water Content on Silica Gel for the Isolation of Interfacial Material from Athabasca Bitumen. *Energy Fuels* **2015**, *29* (11), 7150−7155.
(45) Zito, P.; Chen, H.; Podgorski, D. C.; McKenna, A. M.; Tarr, M. A. Sunlight Creates Oxygenated Species in Water-Soluble Fractions of Deepwater Horizon Oil. *J. Hazard. Mater.* **2014**, *280*, 636−643.
(46) Niles, S. F. Fourier-Transform Ion Cyclotron Resonance Mass Spectrometry (FT-ICR MS) for Characterization of Oxygenated Fossil Fuels in the Environment. Ph.D. Thesis, Florida State University, 2020.
(47) Smith, D. F.; Podgorski, D. C.; Rodgers, R. P.; Blakney, G. T.; Hendrickson, C. L. 21 T FT-ICR Mass Spectrometer for Ultrahigh-Resolution Analysis of Complex Organic Mixtures. *Anal. Chem.* **2018**, *90* (3), 2041−2047.
(48) Blakney, G. T.; Hendrickson, C. L.; Marshall, A. G. Predator Data Station: A Fast Data Acquisition System for Advanced FT-ICR MS Experiments. *Int. J. Mass Spectrom.* **2011**, *306* (2−3), 246−252.
(49) Xian, F.; Hendrickson, C. L.; Blakney, G. T.; Beu, S. C.; Marshall, A. G. Automated Broadband Phase Correction of Fourier Transform Ion Cyclotron Resonance Mass Spectra. *Anal. Chem.* **2010**, *82* (21), 8807−8812.
(50) Corilo, Y. E. *PetroOrg Software*; Omics LLC: Tallahassee, FL, 2014.
(51) Kendrick, E. A Mass Scale Based on CH_2 = 14.0000 for High Resolution Mass Spectrometry of Organic Compounds. *Anal. Chem.* **1963**, *35* (13), 2146−2154.
(52) McLafferty, F. W. *Interpretation of Mass Spectra*, 3rd ed.; Turro, N. J., Ed.; University Science Books: Mill Valley, 1980.
(53) Boduszynski, M. M. Composition of Heavy Petroleums. 2. Molecular Characterization. *Energy Fuels* **1988**, *2* (5), 597−613.
(54) McKenna, A. M.; Purcell, J. M.; Rodgers, R. P.; Marshall, A. G. Heavy Petroleum Composition. 1. Exhaustive Compositional Analysis of Athabasca Bitumen HVGO Distillates by Fourier Transform Ion Cyclotron Resonance Mass Spectrometry: A Definitive Test of the Boduszynski Model. *Energy Fuels* **2010**, *24* (5), 2929−2938.
(55) Rojas-Ruiz, F. A.; Orrego-Ruiz, J. A. Distribution of Oxygen-Containing Compounds and Its Significance on Total Organic Acid Content in Crude Oils by ESI Negative Ion FT-ICR MS. *Energy Fuels* **2016**, *30* (10), 8185−8191.
(56) Glattke, T. J.; Chacón-Patiño, M. L.; Marshall, A. G.; Rodgers, R. P. Maltene and Asphaltene Contributions to the Formation of Water-Soluble Emerging Contaminants from Photooxidation of Paving Materials. *Energy Fuels* **2022**, *36* (21), 13060−13072.
(57) Ballard, D. A.; Chacón-Patiño, M. L.; Qiao, P.; Roberts, K. J.; Rae, R.; Dowding, P. J.; Xu, Z.; Harbottle, D. Molecular Characterization of Strongly and Weakly Interfacially Active Asphaltenes by High-Resolution Mass Spectrometry. *Energy Fuels* **2020**, *34* (11), 13966−13976.

https://doi.org/10.1021/acs.energyfuels.4c03107
Energy Fuels 2025, 39, 1031−1041